Nanoscale

ROYAL SOCIETY OF CHEMISTRY

COMMUNICATION

View Article Online
View Journal | View Issue

Cite this: *Nanoscale*, 2020, **12**, 18606

Received 15th July 2020,
Accepted 23rd August 2020

DOI: 10.1039/d0nr05281g

rsc.li/nanoscale

Hybrid nanocapsules for *in situ* TEM imaging of gas evolution reactions in confined liquids†

Sardar B. Alam, [a,b] Jiwoong Yang,‡[b] Karen C. Bustillo, [a] Colin Ophus, [a] Peter Ercius, [a] Haimei Zheng *[b,c] and Emory M. Chan *[a]

Liquid cell transmission electron microscopy (TEM) enables the direct observation of dynamic physical and chemical processes in liquids at the nanoscale. Quantitative investigations into reactions with fast kinetics and/or multiple reagents will benefit from further advances in liquid cell design that facilitate rapid *in situ* mixing and precise control over reagent volumes and concentrations. This work reports the development of inorganic–organic nanocapsules for high-resolution TEM imaging of nanoscale reactions in liquids with well-defined zeptoliter volumes. These hybrid nanocapsules, with 48 nm average diameter, consist of a thin layer of gold coating a lipid vesicle. As a model reaction, the nucleation, growth, and diffusion of nanobubbles generated by the radiolysis of water is investigated inside the nanocapsules. When the nanobubbles are sufficiently small (10–25 nm diameter), they are mobile in the nanocapsules, but their movement deviates from Brownian motion, which may result from geometric confinement by the nanocapsules. Gases and fluids can be transported between two nanocapsules when they fuse, demonstrating *in situ* mixing without using complex microfluidic schemes. The ability to synthesize nanocapsules with controlled sizes and to monitor dynamics simultaneously inside multiple nanocapsules provides opportunities to investigate nanoscale processes such as single nanoparticle synthesis in confined volumes and biological processes such as biomineralization and membrane dynamics.

Liquid cell transmission electron microscopy (TEM)[1,2] enables the *in situ* observation of dynamic nanoscale processes in their native liquid environments. Liquid cell TEM has been used to observe colloidal synthesis[3,4] and etching of nanoparticles,[5,6] electrochemical deposition,[7,8] biomineralization,[9–11] and cellular dynamics,[12,13] with high spatial and temporal resolution unmatched by optical and X-ray microscopy. Most *in situ* liquid phase TEM studies have been achieved through the development of liquid cells that sandwich a thin layer of reaction solution (10–500 nm thick) between two electron-transparent membranes,[1,2] typically silicon nitride,[14] graphene,[15–17] or carbon films.[18,19] Other approaches to confine liquids include using graphene scrolls[20] or random encapsulation of reaction solutions in capped carbon nanotubes.[21,22] With these advances in liquid cells, it is now possible to reveal reaction dynamics in liquids with atomic resolution. Quantitative studies in this realm, however, will increasingly require liquid cells with precise control over reaction parameters such as reaction volumes, reagent concentrations, and mixing times. While advanced nanofabricated devices[23,24] can produce liquid volumes with well-defined dimensions (*e.g.*, by eliminating silicon nitride membrane bulging under vacuum),[14,25] sample concentrations still can vary unpredictably over time due to solvent evaporation during sample loading or imaging[3] and due to the difficulty of mixing reagents[9] on demand in nanometer-sized liquid cells.

To overcome the challenge of manipulating chemicals in confined environments, cells and organisms transport biomaterial inside lipid vesicles,[26,27] whose self-assembled lipid bilayers encapsulate an aqueous core. Likewise, synthetic lipid vesicles, called liposomes,[28] offer a facile method for confining zeptoliter (1 zL = 10^{-21} L) volumes of reagent solutions with known concentration. These liposomes are routinely used to encapsulate, deliver, and release drugs[29] and have been employed as nanoreactors to confine chemical reactions.[30–33] Established procedures such as extrusion[28] can produce monodisperse size distributions of liposomes as small as 30 nm in diameter.[34] Liposomes can be loaded with reagents simply by assembling the vesicles in the desired reagent solutions.[28] Liposomes containing complementary reagents can be

[a]*The Molecular Foundry, Lawrence Berkeley National Laboratory, Berkeley, CA 94720, USA. E-mail: emchan@lbl.gov*
[b]*Materials Sciences Division, Lawrence Berkeley National Laboratory, Berkeley, CA 94720, USA. E-mail: hmzheng@lbl.gov*
[c]*Department of Materials Science and Engineering, University of California, Berkeley, CA 94720, USA*

†Electronic supplementary information (ESI) available. See DOI: 10.1039/d0nr05281g

‡Present Address: Department of Energy Science and Engineering, Daegu Gyeongbuk Institute of Science and Technology, Daegu 72988, Republic of Korea.

ruptured[35,36] or merged on demand[30,37,38] to rapidly initiate multi-component reactions. For example, the synthesis of CdS nanoparticles has been initiated by fusing microscale liposomes, with simultaneous imaging using *in situ* optical microscopy.[30] In a similar manner, sub-1 μm liposomes could be used as electron-transparent vessels for controlling and imaging nanoscale reactions in TEM liquid cells. Towards the latter objective, empty liposomes 50 to 300 nm in diameter,[39–41] along with other soft colloids like polymeric micelles[42,43] and vesicles,[44] have been imaged with liquid cell TEM. Due to potential electron beam damage, however, it remains a challenge to utilize these soft colloids as nanoreactors for hosting reactions for high resolution *in situ* TEM imaging.

In this work, we prepare liposome-based nanocapsules for *in situ* TEM imaging of reaction dynamics in zeptoliter solutions with high spatial and temporal resolution. Our initial experiments utilized conventional liposomes synthesized *via* the facile and well-established dry lipid film dispersion method,[28] using POPC (1-palmitoyl-2-oleoyl-*sn-glycero*-3-phosphocholine) lipids with 20 mol% cholesterol added to increase bilayer membrane cohesion and mechanical stiffness.[45] Uniform liposomes with average diameters of 35–60 nm were generated, as confirmed with dynamic light scattering (Fig. S1†), by extruding the rehydrated lipids repeatedly through polycarbonate membranes with 50 nm pores. We targeted liposomes of this size because they are sufficiently large to encapsulate colloidal reactions while being sufficiently small to limit liposome deformation on substrates.[46,47] For *in situ* liquid phase TEM imaging, aqueous suspensions of the liposomes were sandwiched between two graphene[15] or amorphous carbon films[18,19] (Fig. 1a and b), producing pockets of the liquid solution in the liquid cell (Fig. S4†). Additional details on sample and liquid cell preparation are provided in the ESI.†

Fig. 1c shows POPC/cholesterol liposomes suspended in water inside a graphene liquid cell (see also Fig. S2†). The thickness of the liposome walls was measured to be *ca.* 3 nm, which is consistent with the expected 2.99 nm thickness of a POPC bilayer with cholesterol.[48] The observed liposomes were sparse, which could be due to the hydrophobic graphene surfaces disrupting the lipid bilayers,[49] especially when compressed by the strong van der Waals forces that seal the graphene cells. The liposomes were also sensitive to electron beam exposure, denaturing under a moderate electron dose rate around 250 e^{-} $Å^{-2}$ s^{-1} (Fig. S3†). This is consistent with other reports that observed soft materials only under low-dose conditions, with typical dose rates below 10 e^{-} $Å^{-2}$ s^{-1}.[12,40,42–44,50] Under such low-doses, it is difficult to achieve sufficient image contrast to resolve reaction dynamics inside the liposomes with high spatial and temporal resolution.[51]

We increased the number of observable liposomes by constructing cells from carbon membranes[18,19] (Fig. 1a), hypothesizing that they could offer more favorable substrates for liposomes compared to graphene liquid cells while retaining the electron transparency of graphene. We also reasoned that coating the liposome bilayers with a thin layer of gold (Fig. 1b) would produce hybrid organic/inorganic nanocapsules that could withstand moderate to high dose rates. To test this hypothesis, we produced hybrid Au-coated POPC liposomes[52–54] by hydrating dry lipid films in aqueous solutions of chloroauric acid (0.1–0.5 mg ml^{-1} $HAuCl_4$) and then extruding the resulting suspension. We imaged the resulting Au-liposome hybrids, shown in Fig. 1d, in liquid cells fabricated from amorphous carbon membranes[18] (cell assembly described in Fig. S4†) and using an aberration-corrected Thermo Scientific Themis TEM operating at 300 kV with electron beam dose rates ranging from 100 to 2000 e^{-} $Å^{-2}$ s^{-1}. The walls of the nanocapsules are clearly visible despite the background of the carbon membranes and surrounding liquid (Fig. 1d). We observed extensive arrays of these "nanocapsules", 35–60 nm in diameter, in a single field of view (Fig. S7†). Most of the nanocapsules encapsulated in the graphene and carbon liquid cells are circular (Fig. S7 and S8a, b†) with size comparable to the DLS *ex situ* measurements and with wall thickness in range of 3–4 nm (Fig. S8c†). The Fast Fourier Transform (FFT) of the TEM image of the liposomes shown in Fig. 1d displays reflections consistent with the 2.04 Å spacing of Au (200) lattice planes (Fig. 1e). The Fourier-filtered image (Fig. 1f), produced by inverting the masked FFT around these reflections, shows that Au(0) covers the entire area of both liposomes. This analysis suggests that Au^{3+} ions are reduced on the lipid bilayers,[40,55] resulting in a thin uniform Au(0) coating on each liposome. In addition to these coatings, some TEM images (Fig. 2a and ESI Movie 1†) occasionally show dark spots, 3 to 7 nm in diameter, suggesting that gold nanoparticles can also nucleate under the electron beam inside or near the nanocapsules.[55]

Fig. 2a and ESI Movie 1† show the dynamics inside eight nanocapsules over the course of 953 s, or over 15 minutes. The nanocapsules do not move, suggesting they are in contact with one or both carbon membranes of the liquid cell. The fixed positioning of the nanocapsules allows the interior dynamic processes to be imaged over an extended period of time. The Au-coated liposomes remained intact for over 15 minutes under electron beam dose rates of 190–730 e^{-} $Å^{-2}$ s^{-1} (Fig. 3a and b). No visible degradation of the nanocapsule walls was observed, in contrast to the observed damage to uncoated liposomes under comparable electron beam dose. We note that previous studies reported imaging of Au-nanoparticle-stained liposomes at a maximum dose rate of 6 e^{-} $Å^{-2}$ s^{-1}.[40] We postulate that the conformal Au coating on the lipid bilayer (Fig. 1f) forms a Au cast of the soft liposome template, which helps the nanocapsule retain its geometry and cargo despite radiolysis and knock-on damage to the underlying lipid bilayer under high electron dose rates. This 2–4 nm Au coating is thin enough to limit the generation of secondary electrons such that the theoretically predicted enhancement of reactive radiolysis products near the Au–water interface[56] may be relatively minor. The conductive carbon membrane windows of the liquid cell can also reduce beam damage[57,58] to the liposomes by reducing electrostatic charging effects, minimizing second-

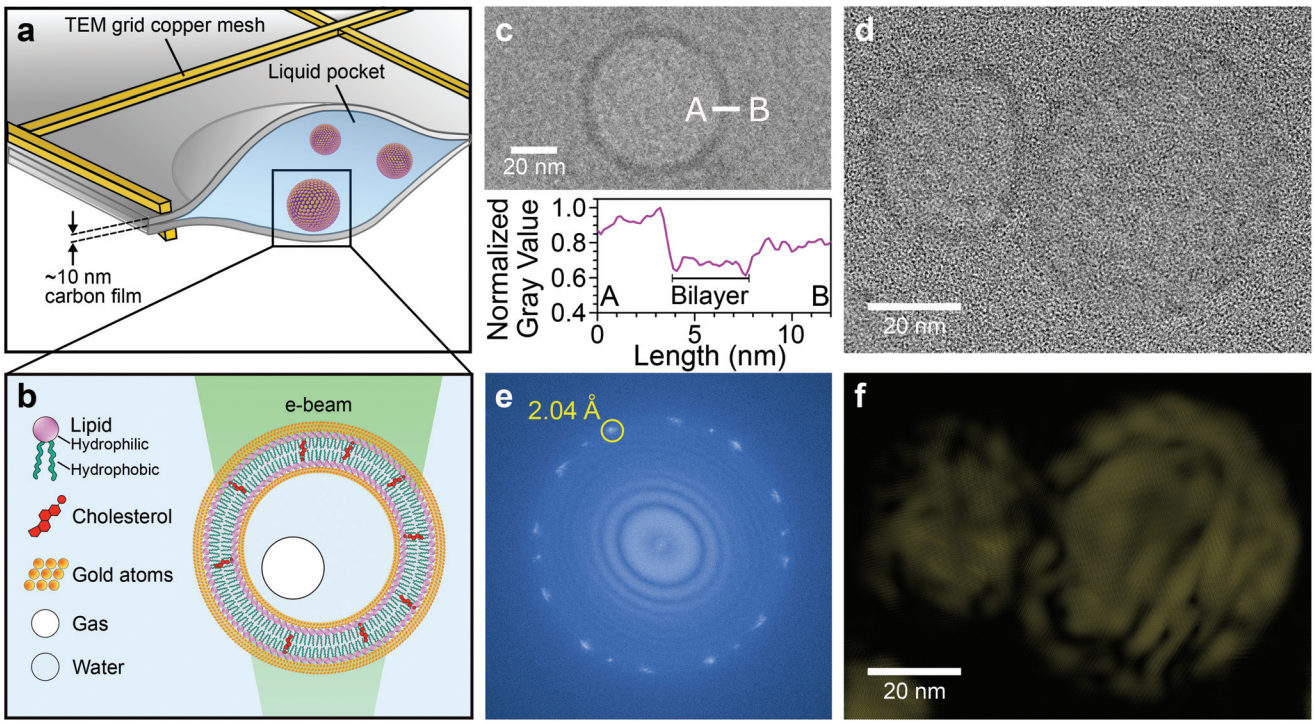

Fig. 1 Au-coated liposome nanocapsules for liquid cell TEM. (a) Schematic of nanocapsules in a TEM liquid cell. (b) The nanocapsules are composed of a Au shell formed on a soft liposome scaffold composed of lipid bilayer and cholesterol molecules in 80 : 20 mol%. During TEM imaging, the e-beam induced radiolysis of water results in gaseous by-products that form bubbles in the capsules' liquid interior. (c) TEM image of liposome scaffold without Au atoms in a graphene liquid cell and intensity profile along line AB showing the *ca.* 3 nm thickness of the lipid bilayer. (d) TEM image of gold-coated, liposome-based nanocapsules in a carbon liquid cell and its corresponding (e) FFT image showing spots corresponding to the 2.04 Å spacing of Au (002) lattice planes. (f) Fourier-filtered image from (d) showing the Au coverage on the liposomes. This image was produced by inverse FFT of the masked spots in (e) corresponding to Au (002) lattice planes.

ary electron yield,[56] and actively scavenging radicals formed by radiolysis of water.[59,60] Further studies on the stability of nanocapsules may shed light on the interaction between the Au coating and the lipid bilayer and their response to high electron beam (e-beam) dose rates.

During imaging, gas bubbles evolved, expanded, and diffused within the 35–60 nm nanocapsules (Fig. 2 and ESI Movie 1†). The evolution and movement of nanoscale bubbles in each nanocapsule confirms the presence of liquid inside the nanocapsules. The observation of moving nanobubbles in the Au-coated liposomes highlights the ability of the nanocapsules to facilitate observation of the dynamics of encapsulated reactions. In this case, the reaction is the radiolysis of water into radical and other molecular species, as described below:[61,62]

$$H_2O \rightarrow eh^-, H^\bullet, OH^\bullet, OH^-, H_2, HO_2^\bullet, H_2O_2, H_3O^+$$

It has been postulated that the bubbles generated during *in situ* TEM of aqueous solutions primarily contain H_2;[55] O_2 may also be present, although it has higher solubility in water than H_2 and takes longer to form compared to primary byproducts of radiolysis. Generally, bubbles are not desired during *in situ* experiments and their formation inside nanocapsules can be avoided by imaging at low dose rates.[39–41] However, here we opted to study the evolution of nanobubbles as a model reaction, because there are a number of advantages this system can offer. For instance, the high contrast of the nanobubbles facilitates automated tracking (Fig. S5†), their size indicates the extent of radiolysis reactions, and their expansion allows us to test the mechanical stability of the nanocapsules. Furthermore, nanobubbles are commonly found in nature, industrial processes, and in therapeutic and diagnostic applications.[63] Therefore, the direct imaging of nanobubbles in liposomes could reveal application-relevant behavior such as the nucleation[64] and stability of nanobubbles near interfaces and within confined spaces.[65]

In addition to formation of bubbles, the reactive by-products of water radiolysis[62] can attack organic functional groups in liposomes.[41] For instance, hydroxyl radicals ($OH^\bullet$) cause hydrogen abstraction, oxidative degradation and formation of radical anions on lipids that can facilitate complexation with free metal cations in the solution.[41] Hence, lipids could sequester ions meant for chemical reactions and could subsequently serve as nucleation sites. Such beam effects can be mitigated by careful management of dose rates and beam exposure – only using higher doses when minimizing noise is critical. The exposure times become relevant as most processes

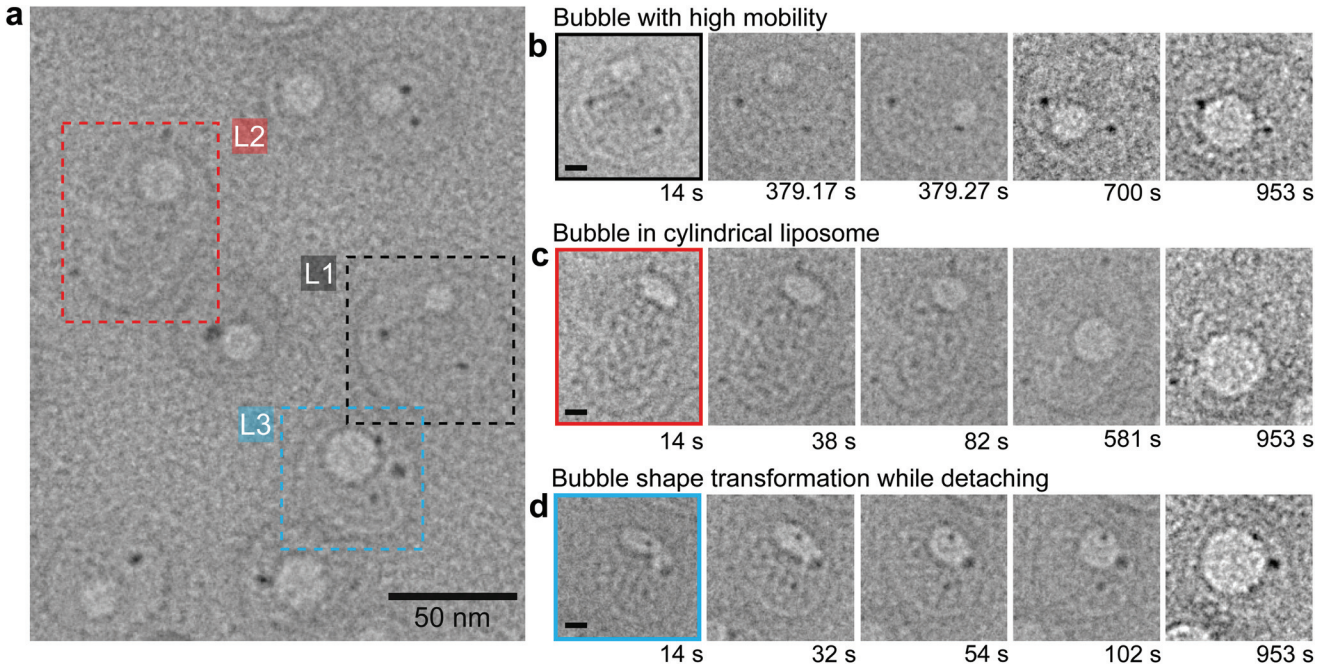

Fig. 2 Observations of nanobubbles in nanocapsules formed by e-beam-induced radiolysis of water. (a) TEM micrograph of eight nanocapsules corresponding to t = 380 s of ESI Movie 1.† Time sequence of nanobubble growth and movement in nanocapsules L1, L2 and L3 marked by (b) black (c) red and (d) blue boxes in (a), respectively. At t = 14 s the bubbles are not circular and are pinned to the nanocapsule walls. The shapes of the bubbles transform into spheres as bubble growth progresses. This is most obvious in (d) from 14 to 102 s. The spherical bubbles detach from the walls and proceed to move to different parts of the nanocapsule. Scale bar for (b), (c) and (d) is 10 nm.

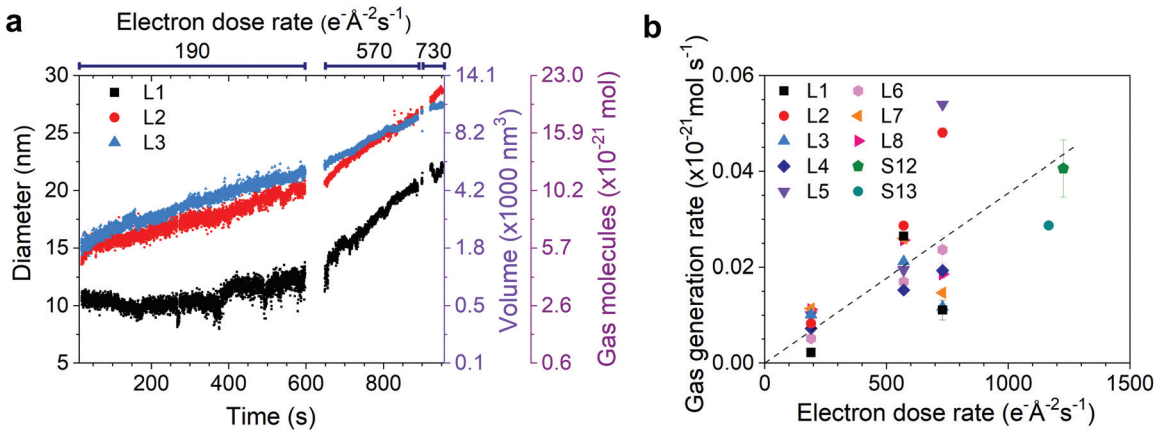

Fig. 3 Growth of gas bubbles by e-beam-induced radiolysis of water. (a) Temporal evolution of the diameter, volume and number of gas molecules in nanobubbles in nanocapsules L1, L2 and L3 from Fig. 2a. The electron dose rate was changed in three steps: 190, 570 and 730 e^- Å^{-2} s^{-1}. With each increase of dose rate, we observe a faster growth rate which indicates higher gas generation rate. This rate is plotted in (b) as a function of electron dose rate. Nanocapsules L4 to L8 are from Fig. 2a and marked in Fig. S11.† Growth rate plots for additional liposomes are shown in Fig. S12 and S13.† The slope of the linear fit is 4 × 10^{-26} mol s^{-1} per e^- Å^{-2} s^{-1}.

like mixing[66] and nanoparticle synthesis[30] take only a few seconds to complete in confined environment of liposomes. Other strategies to minimize beam damage[61] include tuning the solution chemistry, for example, by establishing specific pH levels to lower the steady state concentration of reactive species like hydrated electrons and hydroxyl radicals[62] or by introducing radical scavengers[59,67] into the reaction volume.

For a given electron dose rate, we found that the diameters of nanobubbles in liposomes grow monotonically (Fig. 3a). Assuming a spherical bubble morphology, we calculate the internal pressure P and volume V of each nanobubble and investigate their dependence on the e-beam dose (Fig. 3a and b; see more details in section 6 of the ESI†). We used the ideal gas law ($PV = nRT$) to estimate the moles of gas molecules n

generated at different dose rates (for H_2 at temperatures and pressures used in this work, deviations from ideal behavior are <10%,[68] comparable to the uncertainty in V). We assumed a temperature T of 296.15 K and estimated P using the Young–Laplace equation, $\Delta P = 2\gamma/r$, where r is the bubble radius (P *vs.* time t shown in Fig. S9†). For the surface tension γ, we used the reported value for a monolayer of lipids (~30 mN m^{-1}) at an air–hydrocarbon interface[69,70] as we expect lipids in the nanocapsule to coat the nanobubble. As the dose rate was increased stepwise from 190 to 570 and 730 e^- $Å^{-2}$ s^{-1}, we observed an approximately linear increase in volumetric growth rates of 4, 16 and 24 nm^3 s^{-1}, respectively (Fig. 3a and Fig. S11b†). The linear fit to a plot of nanobubble growth rates *vs.* dose rate (Fig. S11b†) indicates an average volumetric growth rate of 25 $Å^3$ s^{-1} per e^- $Å^{-2}$ s^{-1}, which suggests that the gas generation in the reaction can be controlled at sub-zeptoliter volumes by tuning the electron dose rate. The linear dependence of bubble growth rate on electron dose rate is physically reasonable since each incident electron would be expected to give rise to a set yield of gas molecules, assuming the irradiated area is supersaturated with H_2 under steady-state conditions. This assumption is reasonable for this work since previous studies have shown that when an entire liquid volume (*e.g.*, a nanocapsule) is irradiated with a high dose rate, supersaturation and steady state conditions are established within milliseconds[55,62] – far shorter than the image acquisition frame rate (0.1 s per frame).

From the line fit in Fig. 3b, the rate of the addition of gas molecules to each bubble (dn/dt) can be estimated to be on the order of 10^{-23} to 10^{-22} mol s^{-1}, or approximately 1–10 gas molecules per second at 190 e^- $Å^{-2}$ s^{-1}. Assuming that gas molecules are generated throughout the nanocapsule and do not pass through the capsule shell, this rate suggests that 10^6–10^7 incident electrons are required to generate one gas molecule that contributes to bubble growth. Electron-induced bubble growth occurs through a complex mechanism that potentially incorporates a number of reaction pathways, including radiolysis by secondary electrons, and depends on the solubility and diffusion of the gas in the liquid.[55,56,62] Nevertheless, the linear fit in Fig. 3b is a good quantitative indicator for the efficiency of generating gaseous species in an otherwise complex mechanism.

During nanobubble growth, the nanocapsules remained intact, despite the fact that nanobubble expansion should displace the liquid inside the nanocapsules and cause the vesicles to expand. We observe a small increase in the nanocapsule diameter of *ca.* 5% for circular capsules during bubble growth (Fig. 4a, Fig. S14 and Movie S4†), suggesting a pressure-induced expansion of the nanocapsule shell. The Au-coated liposomes do not suffer a catastrophic rupture during bubble expansion, which suggests that the nanocapsule shell, like a lipid bilayer,[71,72] is either elastic or semipermeable to water, or both. The mechanical stability of the Au-coated liposomes is notable because it contrasts with predictions for the bubble-induced rupture of uncoated liposomes, which has been investigated for drug delivery.[36] The semipermeable shell of Au-coated liposomes could be advantageous for liquid cell TEM, since the electron-dose-rate-dependent bubble expansion (0–40 nm^3 s^{-1}, Fig. S11b†) could be used to finely control the flow rate of water pumped out of the nanocapsules (≤40 yL s^{-1}). Such nanopumps would be analogous to the microfluidic pumps driven by expansion and collapse of thermally[73] or electrochemically[74] generated microbubbles.

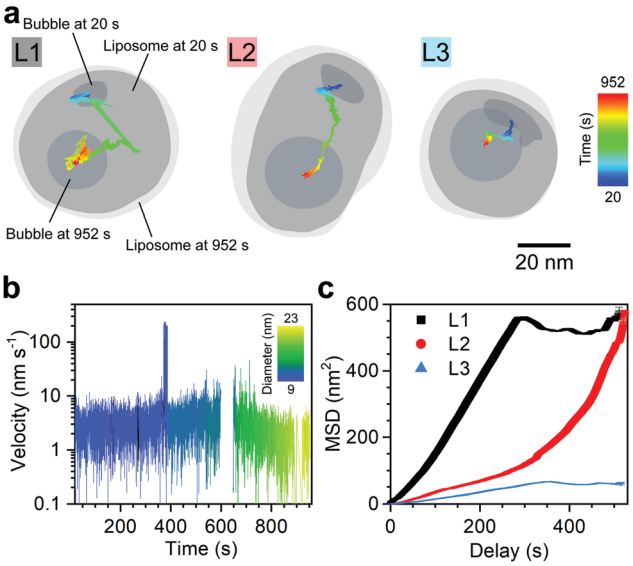

Fig. 4 Movement of bubbles in the interior of nanocapsules. (a) Bubble trajectories for capsules L1, L2 and L3 (Fig. 2a) over time. The initial and final size of the bubbles and nanocapsules are also illustrated. (b) Instantaneous velocity of the bubble in L1 plotted with time, showing rare jumps at a much higher speed of ~200 nm s^{-1} than the typical velocity range of 0 to 5 nm s^{-1}, which decreases with increasing bubble diameter. (c) Time-averaged mean squared displacement (MSD) plots measured for the period starting from bubble detachment from the nanocapsule wall until the electron dose changes at 597 s.

Fig. 2b–d and ESI Movie 1† also show the motion of individual nanobubbles within the confines of the nanocapsules. As shown in Fig. 2b–d and ESI Movie 1,† nanobubbles always formed as small (<15 nm diameter) nuclei in contact with nanocapsule walls. Initially, these bubbles are not spherical, indicating that they are adhered to the interior walls of the nanocapsules. As the bubbles grow, the length of the interface between each bubble and wall remains unchanged, pinned due to the contact angle of the gas/water/lipid interface or due local heterogeneity in the bilayer. Instead, the bubble grows into the interior solution of the nanocapsule and evolves to have a more circular cross section to minimize surface energy. The bubble eventually detaches from the wall, which implies the existence of forces opposing the capillary forces that otherwise make it energetically unfavorable for the bubble to disjoin.[75] The driving force for detachment could arise from spontaneous convection in the interior fluid or from electrostatic repulsion between the e-beam-charged surfaces of the bubble and capsule walls.[76] Both types of forces increase with the expanding surface area of the growing bubble.

After detaching, the nanobubbles diffuse throughout the nanocapsule interior, as demonstrated by the positions and trajectories shown in Fig. 4a. Bubbles in different nanocapsules show various trajectories of motion at early stages. For example, the bubble in nanocapsule L1 (in Fig. 2a) exhibits random motion locally as well as occasional long-range jumps. The bubble in nanocapsule L2 exhibits a more directional trajectory, while the bubble in nanocapsule L3 shows only local fluctuations. While the instantaneous velocities of the nanobubbles in x and y directions ranged mostly from 0.1 to 10 nm s^{-1} (Fig. 4b), bubble velocities occasionally spiked to 200 nm s^{-1} (Fig. 2b, frames 2 and 3; Fig. 4a and b). These long-range jumps could be driven by electrostatic interactions between the e-beam-charged surfaces[77] of nanobubbles and the liposomes. As the bubbles grow over time, the nanocapsules offer effective confinement and restrict bubble mobility. When each bubble completely fills its nanocapsule, the bubble stops growing and moving. However, none of the bubbles escape the confinement of their nanocapsules, demonstrating the ability of the nanocapsules to retain gaseous reaction products.

To characterize the diffusive motion of the nanobubbles in L1, L2 and L3, we investigated the dependence of their mean squared displacement (MSD) on the diffusion time t; such analysis is routinely used to categorize single particle trajectories in liquid cell TEM.[78–80] While traditionally the Brownian motion is defined for a solid sphere, the classical Stokes–Einstein relationship can be modified by a small factor to describe the motion of gas bubbles,[81] thus permitting MSD to characterize bubble diffusion. MSD analysis for short trajectories, as expected in the confined space of nanocapsules, is sensitive to localization error and motion blur.[82] We minimized the localization variance through the use of a custom drift code correction algorithm and careful image segmentation (Fig. S5a†). The MSD traces (Fig. 4c and Fig. S11c†) do not exhibit the linear dependence on t characteristic of simple Brownian motion in bulk liquid across two dimensions (MSD = $4Dt$, where D is the diffusion coefficient).[83] The MSD traces plateau because nanobubbles cannot diffuse outside of the confines of the liposomes, saturating at MSD = 550 nm^2 s^{-1} for the bubble in L1. This saturation value is consistent with the theoretical MSD value of $(R_{capsule} - R_{bubble})^2$ = 484 nm^2 where the radii R for the nanocapsule and bubble are $R_{capsule}$ = 28 nm and R_{bubble} = 6 nm, respectively. Anomalous diffusion is observed even in the linear regions of the MSD plot (Fig. S10b†). The diffusion coefficients extracted from fitting MSD data (0.31, 0.091 and 0.044 nm^2 s^{-1} for bubbles in L1, L2 and L3, respectively) are eight orders of magnitude lower than the Stokes–Einstein diffusivities of spheres with equivalent diameters, suggesting that factors beyond geometric confinement limit nanobubble diffusion in liposomes.

The diffusion of nanobubbles in liposomes may be hindered[84] by electrostatic and hydrodynamic interactions, by crowding[85,86] or spatial heterogeneity in nanocapsules, or by interactions between the nanobubble and the nanocapsule walls. For such anomalous diffusion, the MSD can be described by a power law,[83,86] MSD = $K_\alpha t^\alpha$, where the exponent α defines the different regimes of diffusion, with α = 1 describing classical Brownian motion and K being a time-independent constant with units nm^2 $s^{-\alpha}$. While the diffusion coefficients for all bubbles are several orders of magnitude lower than expected for Brownian motion in water, the exponent α can still be used to differentiate between different class of bubble trajectories. For instance, the three trajectories in Fig. 4a exhibit MSD time traces in two distinct diffusion regimes (Fig. 4c; t^α fits shown in ESI Fig. S10a†). The bubbles in L1 and L3 exhibit $\alpha < 1$, with α = 0.65 and 0.75, respectively, which is consistent with non-directional diffusion in confined geometries[83] and is the prevalent trend for the remaining five liposomes in Fig. 2a as shown in Fig. S11c.† While the bubbles in L1 and L3–L8 all have $\alpha < 1$, the bubbles in the smaller liposomes (L3–L8 with diameters between 35 to 45 nm) are less mobile than the bubble in the larger, 58 nm diameter L1 (MSD in Fig. S11c†). This dependence on geometry is also seen in the bubble in the oblong L2 (with major diameter of 68 nm) with α = 2.75 > 1, which is analogous to super-diffusive behavior[87] caused by its directional trajectory along the length of the nanocapsule (Fig. 4a). Given that liposomes are present in different shapes,[88] liquid cell TEM can facilitate investigations into the effect of nanocontainer geometry on individual nanoparticle entrapment and transport-limited reactions.

Beyond facilitating *in situ* measurements of nanobubble growth and transport, the liposome nanoreactors appear to promote reactions that do not occur as readily in bulk solution. As shown in Fig. 2 and ESI Movie 1,† nanobubbles only form inside the nanocapsules and not in the surrounding fluid. The preferential stability of nanobubbles in nanocapsules could be attributed to the reduction of nanobubble surface tension by a monolayer of lipids coating the bubble.[89–92] The bulk surface tension of an air/water interface coated with a monolayer of POPC (*ca.* 30 mN m^{-1}) is less than half of the 72 mN m^{-1} (ref. 93) surface tension for a bare interface. The amphiphilic lipids thus act as a surfactant and reduce the critical size and free energy barrier required to nucleate a bubble.[94] An alternate explanation for the preferential nucleation of nanobubbles in nanocapsules is that the concentration of dissolved radiolysis products (*e.g.*, H_2) in the fluid outside the nanocapsules cannot reach supersaturation due to rapid diffusion away from the irradiated area.[56] These two mechanisms, if confirmed, would demonstrate that the confinement and distinct chemical environment inside nanocapsules drive selective reaction behavior.

Finally, we observed that the gaseous reaction products can be transported between two nanocapsules. As shown in Fig. 5a, c and ESI Movies 2 and 3,† we observe the merging of two Au-coated liposomes followed by the transport of gas from the smaller bubble to the larger one. The directionality of gas transport is likely driven by the higher internal pressure of the smaller bubble. Before the two nanocapsules in Fig. 5a fuse, they are separated by a minimum distance of only 2.6 nm, highlighting the need for *in situ* TEM to study such fusion processes.[95] The smaller nanocapsule spontaneously forms a protrusion in its shell that locally repels the shell of the larger

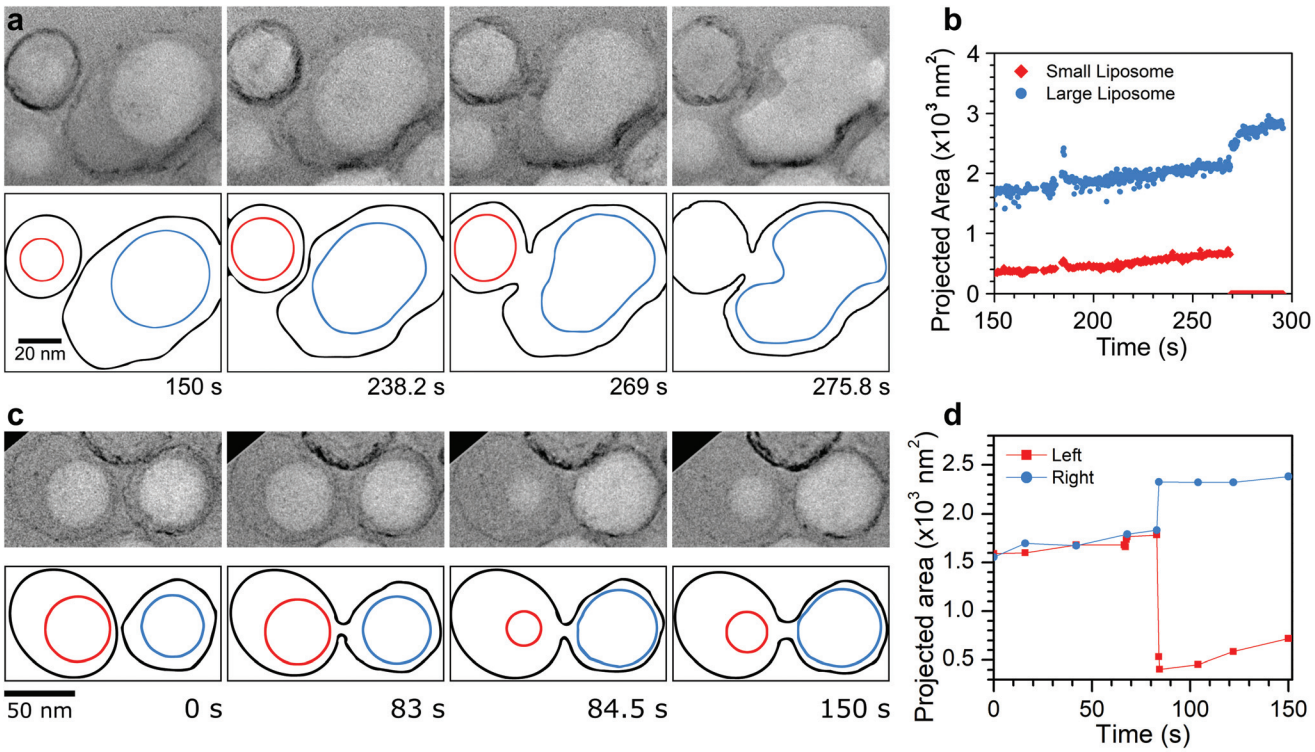

Fig. 5 Gas transport between nanocapsules upon fusion. (a) Frames from ESI Video 2† and corresponding bubble and nanocapsule contours showing gas transport between nanocapsules. At 269 s, fusion between the nanocapsules occurs, and gas from the nanobubble in the smaller capsule is immediately transported to the larger capsule. (b) Projected area of the nanobubbles vs time, showing the sudden increase in size of the larger bubble with a correlated disappearance of the bubble in the smaller nanocapsule. The fluid jet formed at 275.8 s during gas transport from the smaller to the larger nanocapsule, also deforms the bubble. (c) Frames from ESI Video 3† and contour plot showing gas transport between nanocapsules also initiated by fusion. When gas is transferred from the left nanocapsules to the right at 84.5 s, the transferred volume is limited by the space available in the receiving nanocapsules. As the volume of the nanocapsule on right is filled to capacity, some gas remains in the left capsule. (d) Projected area of bubbles in the left and right nanocapsule in (c).

capsule (Fig. 5a, t = 238.2 s). The protrusion of the smaller nanocapsule eventually contacts the shell and induces fusion (269 s). Within one frame (Movie S2†), the bubble in the smaller capsules vanishes with a correlated increase in the projected area of the bubble in the larger capsule (Fig. 5a and b, 275.8 s). Transport of liquid between nanocapsules is also observed during this process (Fig. S18†). The transport of gas between nanocapsules is limited to the available space in the adjacent nanocapsule, as illustrated by Fig. 5c, d and ESI Movie S3;† here, the bubble in the source nanocapsule does not completely vanish since the receiving vesicle cannot accommodate all of the gas from the source bubble. The ability to trigger mixing by fusing liposomes will be useful for *in situ* measurements of fast chemical reactions. These liquid cell TEM experiments would be analogous to liposome-mediated reactions imaged by optical microscopy,[30–32,38] but with orders of magnitude higher spatial resolution. While liposome fusion does not require high electron dose rates and can be initiated at low doses,[40,41] it does require two nanocapsules to be in close proximity. Deterministic approaches for pairing nanocapsules loaded with complementary reactants can be implemented by functionalizing liposomes with lipids of opposite charge,[66] by creating nested structures of liposomes in liposomes,[35,96] or by hydrodynamically trapping[97] liposomes in features patterned on the window membranes. The initiation of reactions in such systems can be triggered not only by e-beam interactions but also by a variety of thermal,[35,98] optical,[99] and electrical[31] stimuli.

Conclusions

In summary, we have utilized gold-coated liposomes as nanocapsules to confine and image nanoscale reactions in zeptoliters of aqueous solution. Using this *in situ* liquid cell TEM approach, we observed the dynamics of nanobubble formation, growth, and movement within 35–60 nm diameter nanocapsules. In addition, the transport of gas between liposomes has also been captured. An understanding of the nanobubble dynamics inside liposome-based nanocapsules is biomedically relevant since liposome-encapsulated bubbles are used as ultrasound contrast agents and as actuators for drug delivery.[36,100–102] Imaging liposomes and other soft colloids in liquid at high resolution can reveal their complex structural response to interactions with different surfaces or changes to their surrounding medium, *e.g.*, ionic strength or pH.[34]

Moving forward, the integration of nanocapsules with liquid cell TEM could facilitate *in situ* observation of a broad range of nanoscale reactions such as hydrogen storage in metal nanoparticles,[103] the growth of single inorganic nanocrystals, and mineralization on lipid bilayers.[104] For such reactions, self-assembled nanocapsules offer a facile approach to simultaneously initiate and observe multiple, isolated reactions in a single field of view, which can be used to rapidly acquire statistics for stochastic processes and screen combinatorial libraries. In contrast, achieving comparable zeptoliter confinement of liquid pockets in top-down nanofabricated liquid cells currently requires resource-intensive e-beam or nanoimprint lithography[105] or requires surface treatments to ensure the fluids are retained in the nano-reservoirs. The ability to visualize the evolution of nanoscale reactions without labor-intensive fabrication will facilitate the direct testing of mechanistic theories, accelerating the development of new materials and helping to elucidate the complex reaction networks that produce them.[106–108]

Conflicts of interest

The authors declare no competing interest.

Acknowledgements

This work was funded by U.S. Department of Energy, Office of Science, Office of Basic Energy Sciences, Materials Sciences and Engineering Division under Contract No. DE-AC02-05-CH11231 within the *in situ* TEM program (KC22ZH). Work at the Molecular Foundry was supported by the Office of Science, Office of Basic Energy Sciences, of the U.S. Department of Energy under Contract No. DE-AC02-05CH11231. The authors thank C. Ajo-Franklin and M. Wang for guidance on working with liposomes, S. Aloni for informative discussions, and D. Han for 3D graphics.

References

1 H.-G. Liao and H. Zheng, *Annu. Rev. Phys. Chem.*, 2016, **67**, 719–747.
2 F. M. Ross, *Science*, 2015, **350**, aaa9886.
3 N. D. Loh, S. Sen, M. Bosman, S. F. Tan, J. Zhong, C. A. Nijhuis, P. Král, P. Matsudaira and U. Mirsaidov, *Nat. Chem.*, 2016, **9**, 77.
4 H.-G. Liao, D. Zherebetskyy, H. Xin, C. Czarnik, P. Ercius, H. Elmlund, M. Pan, L.-W. Wang and H. Zheng, *Science*, 2014, **345**, 916–919.
5 J. Wu, W. Gao, H. Yang and J.-M. Zuo, *ACS Nano*, 2017, **11**, 1696–1703.
6 M. R. Hauwiller, J. C. Ondry, C. M. Chan, P. Khandekar, J. Yu and A. P. Alivisatos, *J. Am. Chem. Soc.*, 2019, **141**, 4428–4437.
7 M. J. Williamson, R. M. Tromp, P. M. Vereecken, R. Hull and F. M. Ross, *Nat. Mater.*, 2003, **2**, 532–536.
8 Z. Zeng, W.-I. Liang, H.-G. Liao, H. L. Xin, Y.-H. Chu and H. Zheng, *Nano Lett.*, 2014, **14**, 1745–1750.
9 M. H. Nielsen, S. Aloni and J. J. D. Yoreo, *Science*, 2014, **345**, 1158–1162.
10 S. Kashyap, T. J. Woehl, X. Liu, S. K. Mallapragada and T. Prozorov, *ACS Nano*, 2014, **8**, 9097–9106.
11 T. M. Stawski, T. Roncal-Herrero, A. Fernandez-Martinez, A. Matamoros-Veloza, R. Kröger and L. G. Benning, *Phys. Chem. Chem. Phys.*, 2018, **20**, 13825–13835.
12 T. Prozorov, T. P. Almeida, A. Kovács and R. E. Dunin-Borkowski, *J. R. Soc., Interface*, 2017, **14**, 20170464.
13 D. B. Peckys and N. de Jonge, *Nano Lett.*, 2011, **11**, 1733–1738.
14 J. R. Dwyer and M. Harb, *Appl. Spectrosc.*, 2017, **71**, 2051.
15 J. M. Yuk, J. Park, P. Ercius, K. Kim, D. J. Hellebusch, M. F. Crommie, J. Y. Lee, A. Zettl and A. P. Alivisatos, *Science*, 2012, **336**, 61–64.
16 J. Yang, S. B. Alam, L. Yu, E. Chan and H. Zheng, *Micron*, 2019, **116**, 22–29.
17 P. M. G. van Deursen, R. I. Koning, V. Tudor, M.-A. Moradi, J. P. Patterson, A. Kros, N. A. J. M. Sommerdijk, A. J. Koster and G. F. Schneider, *Adv. Funct. Mater.*, 2020, **30**, 1904468.
18 C. Zhu, S. Liang, E. Song, Y. Zhou, W. Wang, F. Shan, Y. Shi, C. Hao, K. Yin, T. Zhang, J. Liu, H. Zheng and L. Sun, *Nat. Commun.*, 2018, **9**, 421.
19 Y. Wang, X. Peng, A. Abelson, P. Xiao, C. Qian, L. Yu, C. Ophus, P. Ercius, L.-W. Wang, M. Law and H. Zheng, *Sci. Adv.*, 2019, **5**, eaaw5623.
20 U. Mirsaidov, V. R. S. S. Mokkapati, D. Bhattacharya, H. Andersen, M. Bosman, B. Özyilmaz and P. Matsudaira, *Lab Chip*, 2013, **13**, 2874–2878.
21 Y. Gogotsi, N. Naguib and J. A. Libera, *Chem. Phys. Lett.*, 2002, **365**, 354–360.
22 D. Mattia and Y. Gogotsi, *Microfluid. Nanofluid.*, 2008, **5**, 289–305.
23 M. Tanase, J. Winterstein, R. Sharma, V. Aksyuk, G. Holland and J. A. Liddle, *Microsc. Microanal.*, 2015, **21**, 1629–1638.
24 D. J. Kelly, M. Zhou, N. Clark, M. J. Hamer, E. A. Lewis, A. M. Rakowski, S. J. Haigh and R. V. Gorbachev, *Nano Lett.*, 2018, **18**, 1168–1174.
25 S. Keskin, P. Kunnas and N. de Jonge, *Nano Lett.*, 2019, **19**, 4608–4613.
26 G. Raposo and W. Stoorvogel, *J. Cell Biol.*, 2013, **200**, 373–383.
27 J. S. Bonifacino and B. S. Glick, *Cell*, 2004, **116**, 153–166.
28 P. Walde and S. Ichikawa, *Biomol. Eng.*, 2001, **18**, 143–177.
29 C. Zylberberg and S. Matosevic, *Drug Delivery*, 2016, **23**, 3319–3329.
30 P. Yang, R. Lipowsky and R. Dimova, *Small*, 2009, **5**, 2033–2037.
31 D. T. Chiu, C. F. Wilson, F. Ryttsén, A. Strömberg, C. Farre, A. Karlsson, S. Nordholm, A. Gaggar, B. P. Modi,

A. Moscho, R. A. Garza-López, O. Orwar and R. N. Zare, *Science*, 1999, **283**, 1892–1895.
32 M. I. Khramov and V. N. Parmon, *J. Photochem. Photobiol., A*, 1993, **71**, 279–284.
33 S. Mann, J. P. Hannington and R. J. P. Williams, *Nature*, 1986, **324**, 565–567.
34 J. N. Israelachvili, *Intermolecular and Surface Forces*, Academic Press, 2015.
35 P.-Y. Bolinger, D. Stamou and H. Vogel, *J. Am. Chem. Soc.*, 2004, **126**, 8594–8595.
36 K.-J. Chen, H.-F. Liang, H.-L. Chen, Y. Wang, P.-Y. Cheng, H.-L. Liu, Y. Xia and H.-W. Sung, *ACS Nano*, 2013, **7**, 438–446.
37 T. Robinson, P. E. Verboket, K. Eyer and P. S. Dittrich, *Lab Chip*, 2014, **14**, 2852–2859.
38 A. Rørvig-Lund, A. Bahadori, S. Semsey, P. M. Bendix and L. B. Oddershede, *Nano Lett.*, 2015, **15**, 4183–4188.
39 S. M. Hoppe, D. Y. Sasaki, A. N. Kinghorn and K. Hattar, *Langmuir*, 2013, **29**, 9958–9961.
40 M. Piffoux, N. Ahmad, J. Nelayah, C. Wilhelm, A. Silva, F. Gazeau and D. Alloyeau, *Nanoscale*, 2018, **10**, 1234–1244.
41 K. Gnanasekaran, H. Chang, P. J. M. Smeets, J. Korpanty, F. M. Geiger and N. C. Gianneschi, *Nano Lett.*, 2020, **20**, 4292–4297.
42 L. R. Parent, E. Bakalis, A. Ramírez-Hernández, J. K. Kammeyer, C. Park, J. de Pablo, F. Zerbetto, J. P. Patterson and N. C. Gianneschi, *J. Am. Chem. Soc.*, 2017, **139**, 17140–17151.
43 C. Li, C. C. Tho, D. Galaktionova, X. Chen, P. Král and U. Mirsaidov, *Nanoscale*, 2019, **11**, 2299–2305.
44 A. Ianiro, H. Wu, M. M. J. van Rijt, M. P. Vena, A. D. A. Keizer, A. C. C. Esteves, R. Tuinier, H. Friedrich, N. A. J. M. Sommerdijk and J. P. Patterson, *Nat. Chem.*, 2019, **11**, 320.
45 P. A. Hyslop, B. Morel and R. D. Sauerheber, *Biochemistry*, 1990, **29**, 1025–1038.
46 K. Dimitrievski, *Langmuir*, 2010, **26**, 3008–3011.
47 E. Reimhult, F. Höök and B. Kasemo, *J. Chem. Phys.*, 2002, **117**, 7401–7404.
48 F. A. Nezil and M. Bloom, *Biophys. J.*, 1992, **61**, 1176–1183.
49 Y. Tu, M. Lv, P. Xiu, T. Huynh, M. Zhang, M. Castelli, Z. Liu, Q. Huang, C. Fan, H. Fang and R. Zhou, *Nat. Nanotechnol.*, 2013, **8**, 594.
50 W. J. Dearnaley, B. Schleupner, A. C. Varano, N. A. Alden, F. Gonzalez, M. A. Casasanta, B. E. Scharf, M. J. Dukes and D. F. Kelly, *Nano Lett.*, 2019, **19**, 6734–6741.
51 L. E. Franken, K. Grünewald, E. J. Boekema and M. C. A. Stuart, *Small*, 2020, 1906198.
52 Y. Jin and X. Gao, *J. Am. Chem. Soc.*, 2009, **131**, 17774–17776.
53 T. S. Troutman, J. K. Barton and M. Romanowski, *Adv. Mater.*, 2008, **20**, 2604–2608.
54 L. Luo, Y. Bian, Y. Liu, X. Zhang, M. Wang, S. Xing, L. Li and D. Gao, *Small*, 2016, **12**, 4103–4112.
55 J. M. Grogan, N. M. Schneider, F. M. Ross and H. H. Bau, *Nano Lett.*, 2014, **14**, 359–364.
56 T. Gupta, N. M. Schneider, J. H. Park, D. Steingart and F. M. Ross, *Nanoscale*, 2018, **10**, 7702–7710.
57 J. R. Fryer, *Ultramicroscopy*, 1984, **14**, 227–236.
58 S. M. Salih and V. E. Cosslett, *Philos. Mag.*, 1974, **30**, 225–228.
59 H. Cho, M. R. Jones, S. C. Nguyen, M. R. Hauwiller, A. Zettl and A. P. Alivisatos, *Nano Lett.*, 2017, **17**, 414–420.
60 S. Keskin and N. de Jonge, *Nano Lett.*, 2018, **18**, 7435–7440.
61 T. j. Woehl and P. Abellan, *J. Microsc.*, 2017, **265**, 135–147.
62 N. M. Schneider, M. M. Norton, B. J. Mendel, J. M. Grogan, F. M. Ross and H. H. Bau, *J. Phys. Chem. C*, 2014, **118**, 22373–22382.
63 M. Alheshibri, J. Qian, M. Jehannin and V. S. J. Craig, *Langmuir*, 2016, **32**, 11086–11100.
64 J. R. T. Seddon, D. Lohse, W. A. Ducker and V. S. J. Craig, *ChemPhysChem*, 2012, **13**, 2179–2187.
65 J. Wei, X. Zhang, F. Song and Y. Shao, *J. Chem. Phys.*, 2018, **148**, 064704.
66 S. M. Christensen, P.-Y. Bolinger, N. S. Hatzakis, M. W. Mortensen and D. Stamou, *Nat. Nanotechnol.*, 2012, **7**, 51–55.
67 E. Sutter, K. Jungjohann, S. Bliznakov, A. Courty, E. Maisonhaute, S. Tenney and P. Sutter, *Nat. Commun.*, 2014, **5**, 4946.
68 M. Hirscher, *Handbook of Hydrogen Storage: New Materials for Future Energy Storage*, Wiley-VCH Verlag GmbH & Co. KgaA, Weinheim, 2010.
69 F. Jähnig, *Biophys. J.*, 1996, **71**, 1348–1349.
70 H. Schindler, *FEBS Lett.*, 1980, **122**, 77–79.
71 D. Huster, A. J. Jin, K. Arnold and K. Gawrisch, *Biophys. J.*, 1997, **73**, 855–864.
72 J. C. Mathai, S. Tristram-Nagle, J. F. Nagle and M. L. Zeidel, *J. Gen. Physiol.*, 2008, **131**, 69–76.
73 B. Liu, J. Sun, D. Li, J. Zhe and K. W. Oh, *Microfluid. Nanofluid.*, 2016, **20**, 155.
74 W. Satoh, Y. Shimizu, T. Kaneto and H. Suzuki, *Sens. Actuators, B*, 2007, **123**, 1153–1160.
75 D. Shin, J. B. Park, Y.-J. Kim, S. J. Kim, J. H. Kang, B. Lee, S.-P. Cho, B. H. Hong and K. S. Novoselov, *Nat. Commun.*, 2015, **6**, 6068.
76 M. Q. Raza, N. Kumar and R. Raj, *Sci. Rep.*, 2016, **6**, 19113.
77 E. R. White, M. Mecklenburg, B. Shevitski, S. B. Singer and B. C. Regan, *Langmuir*, 2012, **28**, 3695–3698.
78 J. Lu, Z. Aabdin, N. D. Loh, D. Bhattacharya and U. Mirsaidov, *Nano Lett.*, 2014, **14**, 2111–2115.
79 A. S. Powers, H.-G. Liao, S. N. Raja, N. D. Bronstein, A. P. Alivisatos and H. Zheng, *Nano Lett.*, 2017, **17**, 15–20.
80 X. Fu, B. Chen, J. Tang, M. T. Hassan and A. H. Zewail, *Science*, 2017, **355**, 494–498.
81 S. H. Chen, *J. Colloid Interface Sci.*, 1999, **209**, 31–43.
82 X. Michalet and A. J. Berglund, *Phys. Rev. E: Stat., Nonlinear, Soft Matter Phys.*, 2012, **85**, 061916.
83 R. Metzler and J. Klafter, *Phys. Rep.*, 2000, **339**, 1–77.

84 P. Sharma, S. Ghosh and S. Bhattacharya, *Appl. Phys. Lett.*, 2010, **97**, 104101.
85 R. J. Ellis and A. P. Minton, *Nature*, 2003, **425**, 27–28.
86 D. S. Banks and C. Fradin, *Biophys. J.*, 2005, **89**, 2960–2971.
87 I. M. Tolić-Nørrelykke, E.-L. Munteanu, G. Thon, L. Oddershede and K. Berg-Sørensen, *Phys. Rev. Lett.*, 2004, **93**, 078102.
88 S. Svetina and B. Žekš, *Anat. Rec.*, 2002, **268**, 215–225.
89 D. E. Yount, E. W. Gillary and D. C. Hoffman, *J. Acoust. Soc. Am.*, 1984, **76**, 1511–1521.
90 C. Hernandez, L. Nieves, A. C. de Leon, R. Advincula and A. A. Exner, *ACS Appl. Mater. Interfaces*, 2018, **10**, 9949–9956.
91 C. Hernandez, S. Gulati, G. Fioravanti, P. L. Stewart and A. A. Exner, *Sci. Rep.*, 2017, **7**, 1–8.
92 E. C. Unger, T. Porter, W. Culp, R. Labell, T. Matsunaga and R. Zutshi, *Adv. Drug Delivery Rev.*, 2004, **56**, 1291–1314.
93 N. B. Vargaftik, B. N. Volkov and L. D. Voljak, *J. Phys. Chem. Ref. Data*, 1983, **12**, 817–820.
94 M. Blander and J. L. Katz, *AIChE J.*, 1975, **21**, 833–848.
95 L. V. Chernomordik and M. M. Kozlov, *Nat. Struct. Mol. Biol.*, 2008, **15**, 675–683.
96 N.-N. Deng, M. Yelleswarapu, L. Zheng and W. T. S. Huck, *J. Am. Chem. Soc.*, 2017, **139**, 587–590.
97 A. M. Skelley, O. Kirak, H. Suh, R. Jaenisch and J. Voldman, *Nat. Methods*, 2009, **6**, 147–152.
98 A. Peyret, E. Ibarboure, N. Pippa and S. Lecommandoux, *Langmuir*, 2017, **33**, 7079–7085.
99 J. W. Hindley, Y. Elani, C. M. McGilvery, S. Ali, C. L. Bevan, R. V. Law and O. Ces, *Nat. Commun.*, 2018, **9**, 1093.
100 R. Nahire, M. K. Haldar, S. Paul, A. Mergoum, A. H. Ambre, K. S. Katti, K. N. Gange, D. K. Srivastava, K. Sarkar and S. Mallik, *Biomacromolecules*, 2013, **14**, 841–853.
101 S. Paul, R. Nahire, S. Mallik and K. Sarkar, *Comput. Mech.*, 2014, **53**, 413–435.
102 G. A. Husseini, W. G. Pitt and A. M. Martins, *Colloids Surf., B*, 2014, **123**, 364–386.
103 R. Bardhan, L. O. Hedges, C. L. Pint, A. Javey, S. Whitelam and J. J. Urban, *Nat. Mater.*, 2013, **12**, 905–912.
104 T. Couasnon, D. Alloyeau, B. Ménez, F. Guyot, J.-M. Ghigo and A. Gélabert, *Sci. Adv.*, 2020, **6**, eaaz3125.
105 S. Franssila, *Introduction to Microfabrication*, John Wiley & Sons, 2010.
106 H. Yang, L. S. Hamachi, I. Rreza, W. Wang and E. M. Chan, *Chem. Mater.*, 2019, **31**, 4173–4183.
107 L. S. Hamachi, H. Yang, I. J.-L. Plante, N. Saenz, K. Qian, M. P. Campos, G. T. Cleveland, I. Rreza, A. Oza, W. Walravens, E. M. Chan, Z. Hens, A. C. Crowther and J. S. Owen, *Chem. Sci.*, 2019, **10**, 6539–6552.
108 J. C. Dahl, X. Wang, X. Huang, E. M. Chan and A. P. Alivisatos, *J. Am. Chem. Soc.*, 2020, **142**, 11915–11926.